A COMPRESSION-TO-TENSION STRESS CONVERSION JIG SET AND A DUMBBELL-SHAPED SPECIMEN FOR ARTIFICIALLY INDUCING NECKING DURING A SPLIT HOPKINSON PRESSURE BAR TEST

HYUNHO SHIN[1], GYUNGGEUN SHIN[1], JAEHYUCK LEE[2],
HYUNSUK CHO[2], JUNMOO LEE[1] & KYONG YOP RHEE[2]
[1]Mechanics of Materials and Design Laboratory, Department of Materials Engineering,
Gangneung-Wonju National University, Republic of Korea
[2]Mechanics of Materials and Design Laboratory, Department of Mechanical Engineering,
Kyunghee University, Republic of Korea

ABSTRACT

A jig set was designed to convert compressive stress into tensile stress in a specialized dumbbell-shaped tensile specimen during a split Hopkinson pressure bar (SHPB) test. This setup intended to artificially induce necking during the SHPB test. The functionality of the aforementioned setup, made of 4340 steel, has been investigated using explicit finite element analysis. Two types of dumbbell-shaped specimens were examined: one with a uniform diameter in the tension-receiving section and the other with a reduced central diameter compared to the diameters at its ends. In the case of the uniform diameter specimen, no significant necking occurred until the first pulse passed through it. Conversely, necking occurred in the specimen with the reduced central diameter during the first pulse duration, resulting in higher strain rates, strains and temperatures in the neck region, confirming the effectiveness of the proposed CTC structure. Therefore, if the specimen's constitutive parameters are inversely identified by tracking the bar signals derived from the necking specimen, these parameters are expected to accurately predict the material's deformation behaviour up to higher strain rates, strains and temperatures, in contrast to the parameter set determined from the specimen that did not experience necking.

Keywords: constitutive model calibration, inverse parameter identification, Considère criterion.

1 INTRODUCTION

Two representative variants of split Hopkinson bars (SHB), specifically the split Hopkinson pressure bar (SHPB) [1]–[14] and the split Hopkinson tension bar (SHTB) [15]–[22], are utilized to measure the stress–strain and strain rate–strain curves of various materials at high strain rates, typically ranging from 100 to 10,000 s^{-1}. These curves, along with those obtained at quasistatic strain rates [23], [24], are crucial for calibrating a strain-rate-dependent constitutive model [25]–[27], which is essential for simulating the dynamic deformation behaviour of materials and their structures [28], [29].

The constitutive models have conventionally been calibrated using nonlinear curve fitting of various stress–strain curves measured across a range of strain rates and temperatures. This process presents challenges due to experimental uncertainties and associated costs particularly at high temperatures. Alternatively, calibration can be accomplished by replicating the measured bar signals through repeated simulations until the simulated signals closely align with the measured counterparts, thereby enabling the inverse identification of constitutive parameters from the consistency of the measured and simulated bar signals [30]–[33]. While the simulation-based inverse identification method for the constitutive model is considered both accurate and cost-effective [32], [33], it requires precise calibration of the bar properties, including elastic modulus, Poisson's ratio, and density, before they are input

WIT Transactions on The Built Environment, Vol 215,
www.witpress.com, ISSN 1743-3509 (on-line)
doi:10.2495/SUSI250141

into the simulation. This requirement can be fulfilled by utilizing either the one-dimensional (1D) method [7], [8] or the three-dimensional (3D) method [9], [10].

According to the rationale outlined in Shin et al. [32] and Cho et al. [33], the combination of a compression-to-tension converting (CTC) specimen structure, the SHPB test, and the inverse parameter identification method allows for the benefits of both the SHPB and the SHTB tests to be achieved while mitigating their respective drawbacks. Three key advantages, among others, are as follows: First, the equivalent stress–equivalent plastic strain curve at a quasi-static strain rate, can be obtained suitably even for materials that exhibit necking through standard tensile tests [23], [24]. This curve is crucial for quantifying strain rate dependency by comparing it with the results from SHB tests. Second, the nature of SHPB signals [9], [10], [33], which can be simulated, can be exploited, while SHTB signals are rarely simulated due to the complexities involved in the pulse generation process. Third, the plastically deforming region in the CTC structure is located away from the contact surfaces between the CTC structure and the bars, thereby minimizing the influence of friction on the measured properties [33], [34], particularly the determined constitutive parameters.

Based on the rationale outlined above, we recently calibrated a constitutive model for high-strength steel using a CTC specimen structure, as illustrated in Fig. 1 [32], [33], referred to as the Type I CTC structure. This method involved conducting repeated simulations of the experimentally measured bar signals derived from the CTC specimen structure until the simulated signals closely matched their experimental counterparts.

Figure 1: Type I compression-to-tension (CTC) structure. *i* represents the contact surface to the incident bar (IB) and *t* denotes that to the transmitted bar (TB).

If necking occurs in a CTC structure during the SHPB test, the strain rate, strain, and temperature in the necked region increase significantly [32], [33]. Consequently, if the constitutive parameters are identified by inversely tracking the bar signals derived from the necking CTC structure, these identified parameters will accurately simulate the deformation behaviour of the materials and structures up to higher strain rates, strains, and temperatures. Therefore, achieving necking in a CTC structure is essential.

According to the Considère criterion [35], necking occurs when the strain hardening slope ($d\sigma_t/d\varepsilon_t$) equals or falls below the flow stress (σ_t): $d\sigma_t/d\varepsilon_t \leq \sigma_t$, where σ_t represents the true stress and ε_t signifies the true strain. This equation exclusively considers the properties of a homogeneous material with ideal geometry. However, in the presence of material inhomogeneity or geometric imperfections, these factors can act as local stress concentration sources, leading to necking even if the Considère criterion has not yet been satisfied.

For a homogeneous material with ideal geometry, necking is less likely to occur in materials that exhibit significant strain-hardening behaviour, such as AISI 4340 steel and oxygen-free high-conductivity copper. However, if a geometric flaw is artificially introduced into a CTC structure, it can promote necking in these materials. Introducing a geometric imperfection into the central column, which experiences tensile stress in the Type I CTC structure (see Fig. 1), poses challenges. This requirement limits the applicability of this structure for materials with a high strain-hardening slope, as it is challenging to induce necking during the SHPB test, particularly during the first stress pulse duration.

In the context presented above, we introduce an alternative CTC specimen structure, referred to as the Type II CTC structure, as illustrated in Fig. 2. The most distinctive feature of this structure, compared to Type I, is its ability to artificially introduce a geometric imperfection in the tension-receiving section of the dumbbell-shaped specimen by reducing the central diameter relative to the diameters at its ends. This modification is expected to facilitate artificial necking during SHPB tests, significantly enhancing strain, strain rate, and temperature. The objective of this paper is to numerically verify the capability of inducing necking in the Type II CTC structure during the first pulse duration in SHPB tests, with increased strain rates, strains, and temperatures.

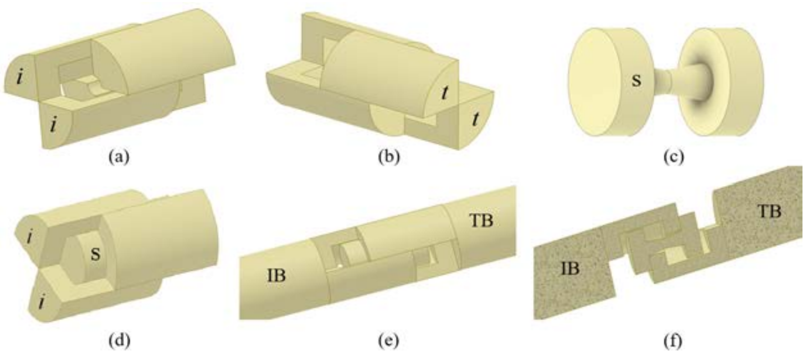

Figure 2: Type II CTC structure. Views of the jig from: (a) the incident bar; and (b) the transmitted bar. (c) Dumbbell-shaped specimen; (d) Assembly of the CTC structure; (e) CTC structure sandwiched between the bars; and (f) Cross-sectional view of the CTC structure and the bars. The symbols *i*, *t*, IB, and TB have the same meanings as those in Fig. 1.

2 NUMERICAL ANALYSIS

A general-purpose finite element (FE) software, ABAQUS Explicit [36], was employed as the solver. The lengths of the striker, incident bar, and transmitted bar were 300 mm, 2,000 mm, and 944 mm, respectively, while the diameter of the formers was 19.05 mm. One quarter of the geometry was modelled with appropriate boundary conditions, taking into account the symmetry of the model. The FE models for two dumbbell-shaped specimens are illustrated in Fig. 3: one with $d = d_c = 3.5$ mm, and the other with $d = 3.5$ mm and $d_c = 3.0$ mm. Here, d represents the end diameter of the tension-receiving section and d_c denotes its central diameter. The length of the CTC assembly is 30 mm.

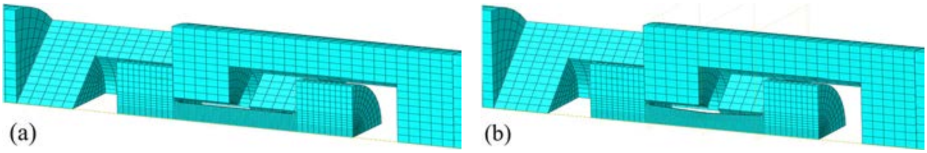

Figure 3: FE models of Type II CTC structures: (a) with $d = d_c = 3.5$ mm; and (b) with $d = 3.5$ mm and $d_c = 3.0$ mm, for the dumbbell-shaped specimen.

Eight-node linear brick elements (C3D8R) were employed to discretize the model space. The mesh sizes of the bar and the portion receiving tension were established through separately conducted mesh size sensitivity test in our previous studies [9], [33]. The initial velocity of the striker, which was initially separated by 0.1 mm from the incident bar, was 15 m/s. A master-slave contact algorithm was applied to all contacting surfaces. A Coulomb friction coefficient of 0.1 was applied to both the surfaces in contact with the CTC structure and the internal surfaces of the CTC structure [33].

Maraging steel was considered for the striker and incident bar, while AA 6061-T6 for the transmitted bar. The density, elastic modulus, and Poisson's ratio of Maraging steel are 8,058.9 kg/m^3, 169.99 GPa and 0.3356, respectively. These values were determined by referencing the authors' calibration results [7]–[10]. The corresponding properties for AA 6061-T6 are 2,700 kg/m^3, 68.9 GPa and 0.33, respectively [37].

AISI 4340 steel was selected as the material for the CTC structure, which comprises the jig and the dumbbell-shaped specimen. Its properties are as follows: a density of 7,830 kg/m^3, an elastic modulus of 200 GPa, a Poisson's ratio of 0.29 and a specific heat capacity of 477 J/kgK. The plastic deformation behaviour is described using the Johnson–Cook model [26]:

$$\sigma = [A + B\varepsilon^n][1 + C \ln \dot{\varepsilon}^*][1 - T^{*m}] \quad (1)$$

where σ represents the equivalent stress, ε denotes the equivalent plastic strain, $\dot{\varepsilon}$ indicates the rate of equivalent plastic strain, and T stands for the current temperature; $\dot{\varepsilon}_0$ is the reference strain rate and T_{ref} is the reference temperature; $\dot{\varepsilon}^* = \dot{\varepsilon}/\dot{\varepsilon}_0$ and $T^* = (T_m - T)/(T_m - T_{ref})$; A, B, n, C, m, and T_m are material constants. The inelastic heat fraction (IHF) was set to one as the configuration variable based on the rationale presented in our previous study [33]. The material parameters used for the simulation are [26]: A = 792 MPa, B = 510 MPa, n = 0.26, C = 0.014, m = 1.03, and T_m=1,793 K (T_{ref}= 298 K, $\dot{\varepsilon}_0$=1 s^{-1}, and IHF = 1).

3 RESULTS AND DISCUSSION

3.1 Bar signals

The strain signals monitored on the surfaces of the incident and transmitted bars, positioned 1,000 mm and 100 mm from the CTC specimen structure, are illustrated in Fig. 4. This figure presents data for two types of dumbbell-shaped specimens: one with $d = d_c$ = 3.5 mm and the other with d = 3.5 mm and d_c = 3.0 mm. While the incident bar signals exhibit relatively minor differences between the two specimen types, the transmitted bar signals demonstrate significant variation. Notably, the magnitudes of all pulses in the incident bar exceed 1,000 μstrain, whereas those in the transmitted bar are approximately 600 μstrain or higher. Since these magnitudes are routinely measured using a metal foil strain gauge in an SHPB experiment, the strain signals derived from the proposed CTC structure can be utilized for the inverse parameter identification of AISI 4340 material. Cho et al. [33] illustrates the sensitivity of the bar signals, particularly the transmitted pulse, to the constitutive parameters of a CTC structure (Type I). This sensitivity was also observed in a separate trial conducted for this study (results not shown). Such sensitivity forms the basis for inverse parameter identification by tracking the bar signals.

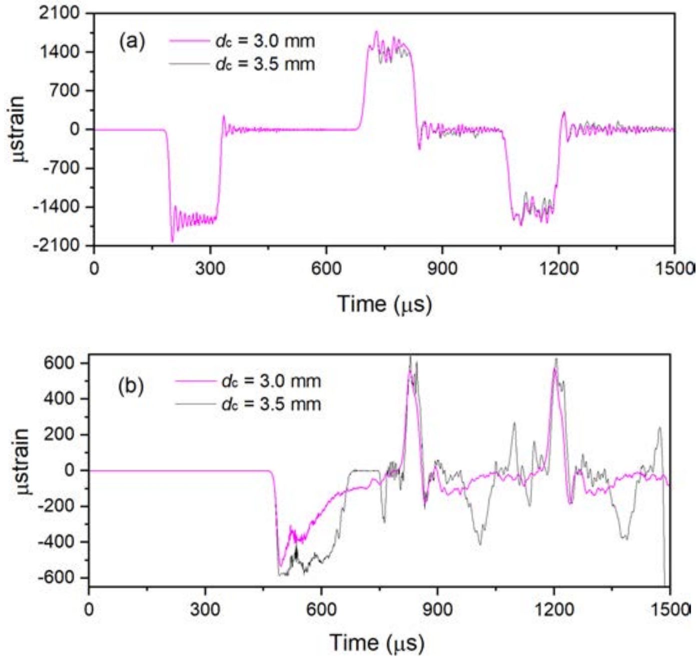

Figure 4: Strain signals on the (a) incident; and (b) transmitted bars during the numerical experiments for the two types of specimens: d = d_c = 3.5 mm and d = 3.5 mm with d_c = 3.0 mm.

3.2 Deformed shapes

The distorted shapes of the two types of CTC structures, along with their equivalent stress contours at 525 μs, are illustrated in Fig. 5. At this point, the dumbbell-shaped specimen with a uniform diameter in the tension-receiving section (Fig. 5(a)) shows no significant necking due to the highly strain-hardening nature of AISI 4340 steel. In contrast, the specimen with a reduced central diameter (Fig. 5(b)) exhibits notable necking. This observation confirms the effectiveness of the proposed CTC structure, which is designed to artificially induce necking during the SHPB test, particularly during the first pulse duration.

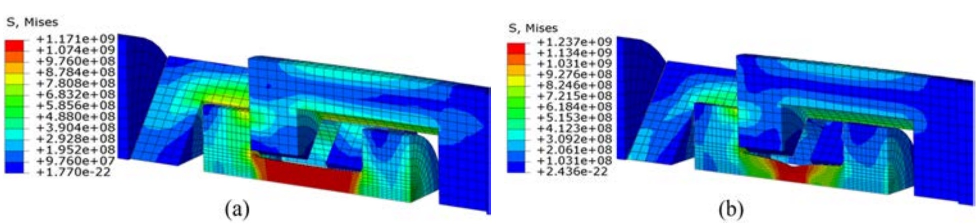

Figure 5: Deformed shapes of the two types of specimens at 525 μs: (a) d = d_c = 3.5 mm; and (b) d = 3.5 mm with d_c = 3.0 mm. The numbers in the legend are expressed in pascals (Pa).

3.3 Strain, strain rate and temperature

The time history of equivalent plastic strain, its time derivative (strain rate), and temperature were also extracted from the central portion of two types of dumbbell-shaped specimens. The results are illustrated in Fig. 6. The specimen exhibiting no apparent necking ($d = d_c$ = 3.5 mm) demonstrates a maximum strain rate of approximately 4,100 s^{-1}, a strain of 0.33, and a temperature of 395 K. In contrast, the specimen exhibiting apparent necking (d = 3.5 mm; d_c = 3.0 mm) experienced a maximum strain rate of approximately 15,000 s^{-1}, a strain of 1.55, and a temperature of 784 K. This observation confirms the effectiveness of the proposed Type II CTC structure. If the constitutive parameters are identified inversely by tracking the bar signals derived from the proposed jig and the dumbbell-shaped specimen with a reduced central diameter, the determined parameters are reliable at least up to the specified strain rate, strain, and temperature. This limit is significantly higher than what can be achieved when identifying parameters using signals derived from a specimen that does not exhibit necking. Our future studies will involve inducing fractures in the neck during the first pulse duration to calibrate a fracture model that is dependent on stress state, strain rate and temperature.

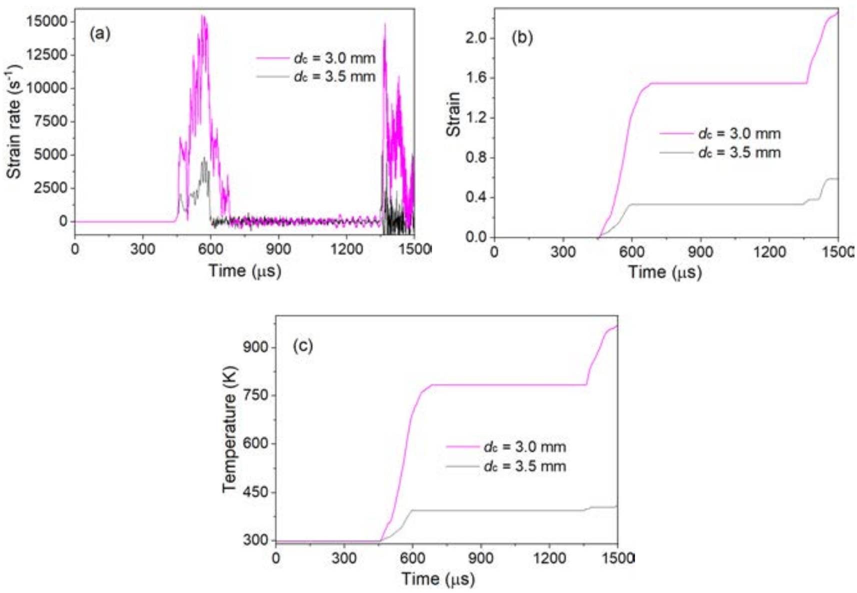

Figure 6: (a) Strain rate; (b) Strain; and (c) Temperature of the dumbbell-shaped specimens: $d = d_c$ = 3.5 mm and d = 3.5 mm with d_c = 3.0 mm.

4 CONCLUSION

A jig set and a specialized dumbbell-shaped specimen were designed for compression-to-tension conversion (CTC) during a split Hopkinson pressure bar (SHPB) test, referred to as the Type II CTC structure. The most distinctive feature of this structure, compared to the Type I CTC structure, is its ability to artificially induce necking. The capabilities of the two types of dumbbell-shaped specimens were investigated using explicit finite element analysis: one with a uniform diameter in the tension-receiving section and the other with a reduced central diameter compared to the diameters at its ends. AISI 4340 steel was selected as the material for both the jig set and the specimen.

When the uniform diameter specimen was subjected to the SHPB test, no significant necking occurred until the first stress pulse passed through it. The specimen experienced a strain rate of approximately 4,100 s^{-1}, a strain of 0.33, and a temperature of 395 K. In contrast, necking was observed in the specimen with the reduced central diameter during the duration of the first pulse. This specimen experienced a strain rate of approximately 15,000 s^{-1}, a strain of 1.55, and a temperature of 784 K. This outcome confirms the effectiveness of the proposed Type II CTC structure. Therefore, it can be concluded that if the specimen's constitutive parameters are inversely identified by tracking the bar signals derived from the necking specimen through repeated simulations, these parameters are expected to accurately predict the material's deformation behaviour up to higher strain rates, strains, and temperatures.

ACKNOWLEDGEMENT

This study was financially supported by the Near-Ideal Split Hopkinson Pressure Bar (NI-SHPB) Program, funded by Dyntech Inc., located in Gangneung, South Korea.

REFERENCES

[1] Kolsky, H., An investigation of the mechanical properties of materials at very high rates of loading. *Proceedings of the Physical Society of London, Section B*, **62**(11), pp. 676–700, 1949. https://doi.org/10.1088/0370-1301/62/11/302.

[2] Zhao, H. & Gary, G., A new method for the separation of waves: Application to the SHPB technique for an unlimited duration of measurement. *Journal of the Mechanics and Physics of Solids*, **45**(7), pp. 1185–1202, 1997. https://doi.org/10.1016/S0022-5096(96)00117-2.

[3] Shin, H. & Kim, J.-B., Evolution of specimen strain rate in split Hopkinson bar test. *Proceedings of the Institution of Mechanical Engineers, Part C: Journal of Mechanical Engineering Science*, **233**(13), pp. 4667–4687, 2019. https://doi.org/10.1177/0954406218813386.

[4] Shin, H. & Kim, D., One-dimensional analyses of striker impact on bar with different general impedance. *Proceedings of the Institution of Mechanical Engineers, Part C: Journal of Mechanical Engineering Science*, **234**(2), pp. 589–608, 2020. https://doi.org/10.1177/0954406219877210.

[5] Shin, H. & Kim, J.-B., Understanding the anomalously long duration time of the transmitted pulse from a soft specimen in a Kolsky bar experiment. *International Journal of Precision Engineering and Manufacturing*, **17**(2), pp. 203–208, 2016. https://doi.org/10.1007/s12541-016-0026-8.

[6] Shin, H., Pochhammer–Chree equation solver for dispersion correction of elastic waves in a (split) Hopkinson bar. *Proceedings of the Institution of Mechanical Engineers, Part C: Journal of Mechanical Engineering Science*, **236**(1), pp. 80–87, 2021. https://doi.org/10.1177/0954406220980509.

[7] Shin, H., Sound speed and Poisson's ratio calibration of (split) Hopkinson bar via iterative dispersion correction of elastic wave. *ASME Journal of Applied Mechanics,* **89**(6), 061007, 2022. https://doi.org/10.1115/1.4054107.

[8] Shin, H., Manual for calibrating sound speed and Poisson's ratio of (split) Hopkinson bar via dispersion correction using Excel and Matlab templates. *Data*, **7**(5), p. 55, 2022. https://doi.org/10.3390/data7050055.

[9] Shin, H., Calibration of bar properties, measured strain, and impact velocity in a bar impact test. *Mechanics of Advanced Materials and Structures*, **31**(24), pp. 6044–6056, 2023. https://doi.org/10.1080/15376494.2023.2224797.

[10] Shin, H., Manual of GUI program governing ABAQUS simulations of bar impact test for calibrating bar properties, measured strain, and impact velocity. *Data*, **8**(3), p. 54, 2023. https://doi.org/10.3390/data8030054.

[11] Shin, H., Lee, H., Kim, J.-B. & Yoo, Y.-H., A numerical verification of the reliability of a split Hopkinson pressure bar with a total bar length of 3 m and a diameter of 1 inch. *Applied Mechanics and Materials*, **799–800**, pp. 681–684, 2015. https://doi.org/10.4028/www.scientific.net/AMM.799-800.681.

[12] Kim, D. & Shin, H., Minimum required distance of strain gauge from specimen for measuring transmitted signal in split Hopkinson pressure bar test. *MATEC Web of Conference*, **308**, 04005, 2020. https://doi.org/10.1051/matecconf/202030804005.

[13] Verleysen, P. & Degrieck, J., Optimized calculation of high strain rate stress–strain curves. *WIT Transactions on the Built Environment*, vol. 98, WIT Press: Southampton and Boston, pp. 369–377, 2008. https://doi.org/10.2495/SU080361.

[14] Verleysen, P., Degrieck, J., Van Slycken, J., De Cooman B. & Samek, L., Experimental investigation of the influence of the specimen geometry on Hopkinson tensile test results. *WIT Transactions on the Built Environment*, vol. 73, WIT Press: Southampton and Boston, pp. 497–505, 2004. https://doi.org/10.2495/SU040461.

[15] Gerlach, P., Kettenbeil, C. & Petrinic, N., A new split Hopkinson tensile bar design. *International Journal of Impact Engineering*, **50**, pp. 63–67, 2012. https://doi.org/10.1016/j.ijimpeng.2012.08.004.

[16] Haugou, G., Leconte, N. & Morvan, H., Design of a pre-stretched tension Hopkinson bar device: Configuration, tail corrections, and numerical validation. *International Journal of Impact Engineering*, **97**, pp. 89–101, 2016. https://doi.org/10.1016/j.ijimpeng.2016.05.018.

[17] Shin, H., Lee, J.-H., Kim, J.-B. & Sohn, S.-I., Design guidelines for the striker and transfer flange of a split Hopkinson tension bar and the origin of spurious waves. *Proceedings of the Institution of Mechanical Engineers, Part C: Journal of Mechanical Engineering Science*, **234**(1), pp. 137–151, 2020. https://doi.org/10.1177/0954406219869984.

[18] Shin, H., Kim, S. & Kim, J.-B., Stress transfer mechanism of flange in split Hopkinson tension bar. *Applied Sciences*, **10**(21), p. 7601, 2020. https://doi.org/10.3390/app10217601.

[19] Nguyen, K.-H., Kim, H.-C., Shin, H., Yoo, Y.-H. & Kim, J.-B., Numerical investigation into the stress wave transmitting characteristics of threads in the split Hopkinson tensile bar test. *International Journal of Impact Engineering*, **109**, pp. 253–263, 2017. https://doi.org/10.1016/j.ijimpeng.2017.07.004.

[20] Kim, Y.-B. & Kim, J. Redesign of split-Hopkinson tensile bar to eliminate spurious wave and verification of strain signal using FEM. *Advanced Mechanical Engineering*, **15**(10), pp. 1–11, 2023. https://doi.org/10.1177/16878132231199843.

[21] Jakkula, P., Cohen, A., Lukić, B., Levi-Hevroni, D., Rack, A., Ganzenmüller, G. & Hiermaier, S., Split Hopkinson tension bar and universal testing machine for high-speed X-ray imaging of materials under tension. *Instruments*, **6**(3), pp. 38, 2022. https://doi.org/10.3390/instruments6030038.

[22] Ruiz-Ripoll, M.L., De Pedraza, V.R. & Roller, C., Influence of the projectile shape on the dynamic tensile characterization of concrete using a split Hopkinson bar. *WIT Transactions on the Built Environment*, vol. 209, WIT Press: Southampton and Boston, pp. 155–166, 2022. https://doi.org/10.2495/HPSU220141.

[23] Shin, H., Kim, S., Choi, M.K. & Ju, Y., Extraction of equivalent stress versus equivalent plastic strain curve of necking material in tensile test without assuming constitutive model. *ASME Journal of Engineering Materials and Technology*, **146**(1), 021037, 2024. https://doi.org/10.1115/1.4064372.

[24] Lee, J., Cho, H., Shin, H., Rhee, K.Y., Kim, W., Lee, H.H., Kim, H.S., Seo, S. & Lee, J., Determination of the equivalent stress–equivalent plastic strain curve of ECAP-processed copper. *Transactions of the Korean Society of Mechanical Engineers, A*, **48**(8), pp. 553–563, 2024. https://doi.org/10.3795/KSME-A.2024.48.8.553.

[25] Shin, H., Ju, Y., Choi, M.-K. & Ha, D.-H., Flow stress description characteristics of some constitutive models at wide strain rates and temperatures. *Technologies*, **10**(2), p. 52, 2022. https://doi.org/10.3390/technologies10020052.

[26] Johnson, G.R. & Cook, W.H., A constitutive model and data for metals subjected to large strains, high strain rates and high temperatures. *Proceedings of the 7th International Symposium on Ballistics*, The Hague, Netherlands, 19–21 Apr., pp. 541–547, 1983.

[27] Shin, H. & Kim, J.-B., A phenomenological constitutive equation to describe various flow stress behavior of materials in wide strain rate and temperature regimes. *ASME Journal of Engineering Materials and Technology*, **132**(2), 021009, 2010. https://doi.org/10.1115/1.4000225.

[28] Shin, H., Lee, H.-J., Yoo, Y.-H. & Lee., W., A determination procedure for element elimination criterion in finite element analysis of high-strain-rate impact/penetration phenomena. *JSME International Journal*, **47**(1), pp. 35–41, 2004. https://doi.org/10.1299/jsmea.47.35.

[29] Kim, J.-B. & Shin, H., NET3D calculation on the depth of penetration by a long-rod penetrator with varying obliquity. *Applied Mechanics and Materials*, **619**, pp. 58–62, 2014. https://doi.org/10.4028/www.scientific.net/AMM.619.58.

[30] Jang, T.J., Kim, J.-B. & Shin, H., Identification of plastic constitutive Johnson–Cook model parameters by optimization-based inverse method. *Journal Computational Design and Engineering*, **8**(4), pp. 1082–1097, 2021. https://doi.org/10.1093/jcde/qwab033.

[31] Lee, J.H., Shin, H., Kim, J.-B., Kim, J.Y., Park, S.T., Kim, G.L. & Oh, K.W., Determination of the flow stress–strain curve of aluminum alloy and tantalum using the compressive load–displacement curve of a hat-type specimen. *ASME Journal of Applied Mechanics*, **86**(3), 031012, 2019. https://doi.org/10.1115/1.4042138.

[32] Shin, H., Cho, H., Lee, J., Lee, J., Shin, G., Rhee, K.Y., Choi, M.K. & Ju, Y., Three types of compression-to-tension stress conversion structures for split Hopkinson pressure bar test for constitutive model calibration in tensile mode. *Abstracts Book of the 14th International Conference on Mechanical and Physical Behaviour of Materials Under Dynamic Loading (DYMAT 2024)*, ETH, Zurich, Switzerland, 9–13 Sep., pp. 254–258, 2024.

[33] Cho, H., Shin, H., Lee, J., Lee, J., Shin, G., Rhee, K.Y., Choi, M.K. & Ju, Y., Constitutive model calibration of high-strength steel in tensile mode using a compression-to-tension stress-converting specimen structure in split Hopkinson pressure bar tests. *Mechanics of Advanced Materials and Structures*, 2025. https://doi.org/10.1080/15376494.2025.2457125.

[34] Shin, H., Lee, J.-H., Kim, J.-B., Seo, S.-J., Lee, J.-G., Lee, J.-O., Yoon, T.-S. & Jung, C.-S., Numerical verification of the Schroeder–Webster surface types and friction compensation models for a metallic specimen in axisymmetric compression test. *ASME Journal of Tribology*, **141**(10), 101401, 2019. https://doi.org/10.1115/1.4044131.
[35] Considère, A., Mémoire sur l'emploi du fer et de l'acier dans les constructions. *Annales des Ponts et Chaussées*, **9**, pp. 574–775, 1885.
[36] Smith, M., ABAQUS/Standard User's Manual, version 6.9, Dassault Systèmes Simulia Corp: Providence, RI, USA, 2009.
[37] MatWeb, Material Property Data. https://matweb.com.